Journal of Alloys and Compounds 502 (2010) 243–249

Contents lists available at ScienceDirect

Journal of Alloys and Compounds

journal homepage: www.elsevier.com/locate/jallcom

Investigation on the structure and properties of $Al_xCr_{1-x}N$ coatings deposited by reactive magnetron co-sputtering

X. Wang [a], L.S. Wang [a], Z.B. Qi [b], G.H. Yue [a], Y.Z. Chen [a], Z.C. Wang [b], D.L. Peng [a,*]

[a] Department of Materials Science and Engineering, College of Materials, Xiamen University, No. 422 Siming South Road, Xiamen 361005, PR China
[b] Department of Chemistry and Chemical Engineering, Xiamen University, Xiamen 361005, PR China

ARTICLE INFO

Article history:
Received 20 March 2010
Received in revised form 8 April 2010
Accepted 21 April 2010
Available online 4 May 2010

Keywords:
$Al_xCr_{1-x}N$ coatings
Vapor deposition
N_2 flow rate
Working pressure
Microstructure
Hardness

ABSTRACT

Al-rich $Al_xCr_{1-x}N$ coatings have been deposited by reactive magnetron co-sputtering using a direct current (DC) power source to Al and a radio frequency (RF) power source to Cr target. The crystal structure, chemical composition, surface morphology, thickness and hardness of the $Al_xCr_{1-x}N$ coatings which were prepared at various N_2 flow rates and working pressures have been systemically investigated. The results show a strong effect of N_2 flow rates and working pressures on the phase composition and microstructure as well as the Al content in $Al_xCr_{1-x}N$ coatings. The present results also show Al contents play an important role in the hardness of the $Al_xCr_{1-x}N$ coatings, which demonstrates the highest hardness for Al contents close to the maximum solubility in cubic $Al_xCr_{1-x}N$.

1. Introduction

Transition metal nitride films have been widely used as protective hard coatings in mechanical and automotive industries due to their high microhardness, excellent wear resistance and superior chemical stability [1–3]. CrN coatings are of outstanding significance for technological applications because they exhibit lower friction coefficient, higher toughness, higher corrosion resistance and wear resistance compared with TiN coatings [4]. However, CrN coatings cannot meet the need of the usage in high speed and dry cutting condition, where the cutting temperature may exceed 1000 °C [5,6]. Recently, great attention has been paid to the Al-rich $Al_xCr_{1-x}N$ coatings. Mayrhofer et al. found that the annealed hexagonal $Al_xCr_{1-x}N$ coatings exhibit beneficial nanoscale-sized domains with CrN precipitates encapsulated in an Al-rich matrix, which makes the coatings more stable at higher temperatures [5]. Very recently, the Al-rich $Al_xCr_{1-x}N$ coatings were successfully prepared by sputtering or evaporating from the AlCr alloy target in $Ar + N_2$ mixed gas atmosphere [7,8]. However, the AlCr alloy target is difficult to be produced by powder sintering technique and its cost is relatively high. A general method to produce the Al-rich $Al_xCr_{1-x}N$ coatings is co-sputtering from Al and Cr targets in $Ar + N_2$ mixed gas atmosphere [9–11], which can also easily obtain coatings with an arbitrary composition. The radio frequency (RF) power is commonly used to Al target in reactive co-sputtering procedure, but the sputtering yield of Al is relatively low in this power mode. The direct current (DC) power can be applied to Al target to enhance the sputtering yield to produce the Al-rich $Al_xCr_{1-x}N$ coatings. However, the sputtering yield of Al target will be greatly affected under this condition, because Al target with a positive chemical activity is rather easy to react with the reactant gas N_2. Therefore, N_2 flow rate and working pressure have become the two most important influencing factors during the above-mentioned reactive co-sputtering process. Several investigations have been preformed on the effect of N_2 flow rate on the preparation of TiAlN coatings by PVD methods [12]; however, little information on the influence of N_2 flow rate and working pressure on the deposition of AlCrN coatings is available.

In this work, in order to investigate the influence of the N_2 flow rate and working pressure on the structure and properties of $Al_xCr_{1-x}N$ coatings deposited by reactive magnetron co-sputtering using a DC power to Al target, the microstructural observation, compositional determination and hardness measurement of the $Al_xCr_{1-x}N$ coatings deposited at different $N_2/(N_2 + Ar)$ ratio (R (N_2)) and working pressure (P_w) have been systemically carried out, and the influential behaviors of N_2 flow

* Corresponding author. Tel.: +86 592 2180155; fax: +86 592 2180155.
E-mail address: dlpeng@xmu.edu.cn (D.L. Peng).

0925-8388/$ – see front matter © 2010 Elsevier B.V. All rights reserved.
doi:10.1016/j.jallcom.2010.04.155

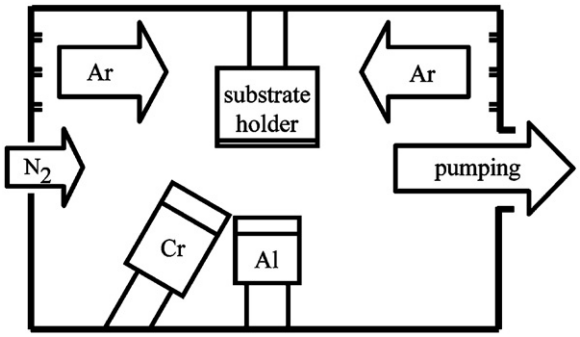

Fig. 1. Schematic drawing of the magnetron co-sputtering system setup in the vacuum chamber for depositing $Al_xCr_{1-x}N$ coatings.

rate and working pressure have been well analyzed and discussed.

2. Experimental details

The $Al_xCr_{1-x}N$ coatings investigated in this study were deposited on glass sheets and Si wafers with the dimension of 12.7 mm × 12.7 mm. All substrates were precleaned by an ultrasonic agitator using acetone and absolute alcohol, respectively, and then dried by inert gases. The substrate holder with a rotational speed of 25 rpm was mounted in the upper part of the chamber. A DC power source sputter gun for Al target was installed right under the substrate holder with a substrate-to-target distance of 9 cm. A RF power source sputter gun for Cr target was installed with an angle of 30° to the vertical axis of the Al target. Both high-purity (99.99 wt.%) Cr and Al targets are 76.2 mm in diameter and 4 mm in thickness. Ar and N_2 were introduced separately into the chamber (Fig. 1). The chamber was pumped down to a base pressure of 1.0×10^{-3} Pa. Before deposition, Ar gas was firstly introduced into the vacuum chamber to pre-sputter for 30 min. Substrate temperature was kept at 300 °C during the whole deposition. The current of Al target (DC) was set at 500 mA and the power of Cr target (RF) was set at 125 W. All the samples were deposited for 1.5 h.

The crystal structure of the $Al_xCr_{1-x}N$ coatings was identified by X-ray diffraction (XRD, Panalytical X'pert PRO) using $Cu_{K\alpha}$ radiation. The microstructural observation and compositional determination of the $Al_xCr_{1-x}N$ coatings were carried out by field-emission scanning electron microscope (FE-SEM, LEO1530) and electron probe microanalyzer (EPMA, JEOL-8100), respectively. The thickness and hardness measurements were performed by surface profiler (Dektak3 Series) and nanoindention tester (CSM), respectively. The indentation depth was always controlled within 1/10th of the total thickness of coatings.

3. Results and discussion

3.1. Effect of N_2 flow rate on $Al_xCr_{1-x}N$ coatings

In order to study the effect of N_2 flow rate on $Al_xCr_{1-x}N$ coatings, the comparable experiments were all carried out at a working pressure of 1.1 Pa. Ar flow rate was fixed at 40 sccm, with $R\,(N_2)$ ranging from 6 to 20%.

3.1.1. XRD and chemical composition analyses

The XRD patterns of $Al_xCr_{1-x}N$ coatings prepared at different $R\,(N_2)$ are presented in Fig. 2, which indicates that most of the coatings show a single B1-NaCl type cubic structure with obviously preferred (1 1 1) orientation, while the coating prepared at $R\,(N_2) = 6\%$ show mixed phases (cubic + hexagonal) (Fig. 2(b)). The growth of (1 1 1)-oriented grains is favored under conditions typical for reactive sputtering deposition [13]. According to the investigation by Gall et al. [13], the energy of incident particle will strongly impact the preferred orientation during reactive sputtering deposition, and the (1 1 1) preferred orientation is commonly induced by the relatively low energetic incident particles which are only metal atoms and N_2 precursors.

The average grain size of the deposited $Al_xCr_{1-x}N$ coatings was calculated from the full width at half maximum (FWHM) in XRD patterns using Scherrer's equation, as shown in Fig. 3, where the average grain size gradually decreases with declining $R\,(N_2)$ from 20 to 6%. The lattice parameter of $Al_xCr_{1-x}N$ coatings calculated

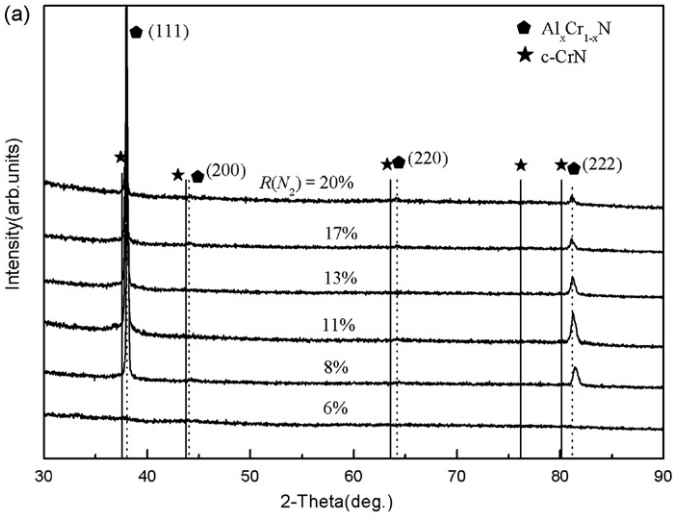

Fig. 2. (a) XRD patterns of $Al_xCr_{1-x}N$ coatings prepared at different $R\,(N_2)$. (b) XRD patterns of $Al_xCr_{1-x}N$ coatings prepared at $R\,(N_2) = 6\%$. *Y*-axis is in logarithmic scale.

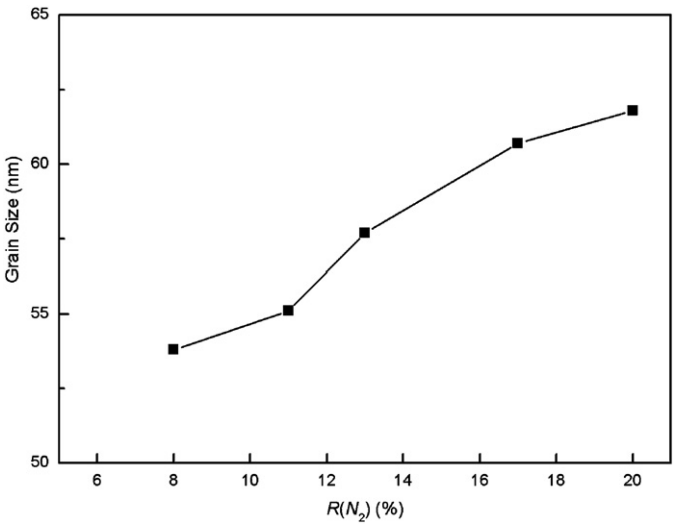

Fig. 3. Grain size of $Al_xCr_{1-x}N$ coatings prepared at different $R\,(N_2)$.

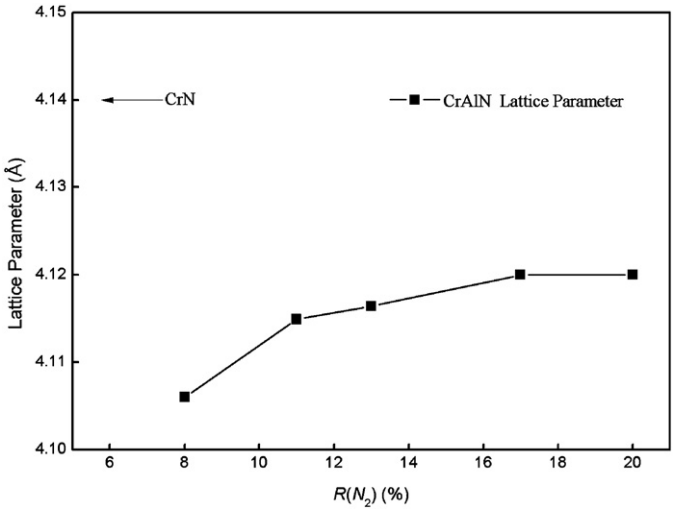

Fig. 4. Lattice parameter of $Al_xCr_{1-x}N$ coatings prepared at different $R\,(N_2)$.

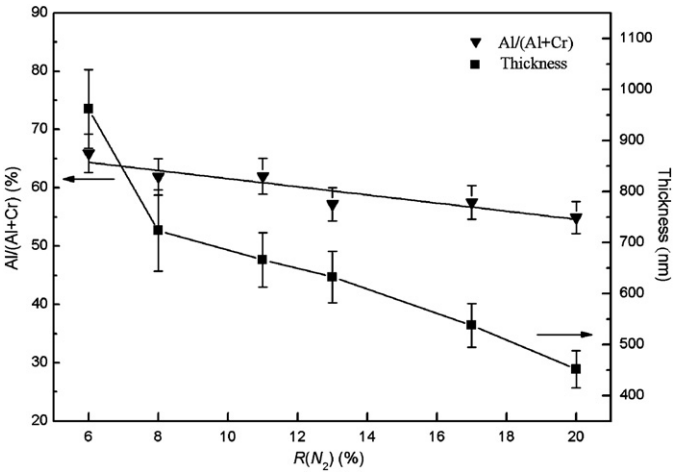

Fig. 5. Al content and thickness of $Al_xCr_{1-x}N$ coatings prepared at different $R\,(N_2)$.

from the above-mentioned XRD patterns decreases, and the lattice parameter of $Al_xCr_{1-x}N$ gradually increases with increasing $R\,(N_2)$ (see Fig. 4). As shown in XRD patterns (Fig. 2), the diffraction peaks of $Al_{1-x}Cr_xN$ slightly shift to lower diffraction angles with increasing $R\,(N_2)$. In addition, as can be seen in Fig. 5, the content of Al atoms with smaller atom radius than Cr atoms decreases with the increase of $R\,(N_2)$. This is mainly attributed to increased poisoning of Al target during reactive sputtering. Under the condition of high $R\,(N_2)$, Al atoms become more difficult to be sputtered due to the formation of a nitride on top of the Al target. Thus, the sputter rate of the Al target decreases, whereas the sputter rate of the Cr target is almost unaffected as it runs with RF mode. Fig. 5 also presents that the thickness of coatings decreases with increasing $R\,(N_2)$, which could partially be attributed to the decreased sputter rate of the Al target as well. In particular, the thickness of coatings jumps from about 962–703 nm when increasing $R\,(N_2)$ from 6 to 8%. According to the XRD patterns in Fig. 2, when $R\,(N_2)$ increases from 6 to 8%, a transformation from mixed phases (cubic + hexagonal) to single phase (cubic) in the structure of coatings can be found. Since the hexagonal phase has about 26% higher specific volume than its cubic phase [14–16], the thickness of coatings sharply decreases with the disappearance of the hexagonal phase.

The compositions of the $Al_xCr_{1-x}N$ coatings determined by EPMA are listed in Table 1. A decrease of N content in $Al_xCr_{1-x}N$ coatings is found with the decrease of $R\,(N_2)$.

3.1.2. Microstructural morphology

SEM images of the surface and cross-section microstructures of the $Al_xCr_{1-x}N$ coatings prepared at various $R\,(N_2)$ are shown in Fig. 6(a)–(f), respectively. As presented in Fig. 6(a), when $R\,(N_2) = 20\%$, the grains of coating with a size of about 60–70 nm have a sharply quadrangular prism shape, and the whole surface of this coating is porous. Moreover, the columnar grain can be clearly seen from the cross-section image of the coating. As $R\,(N_2)$ reduces from 17 to 8% (Fig. 6(b)–(e)), the grains of coatings turn from a coarse four-pyramid shape to a smaller pyramid-like appearance. Accordingly, the coatings become more compact as the pores in the coatings turn smaller, though some bulk grains and pores still exist. When $R\,(N_2)$ reduces to 6% (Fig. 6(f)), no obvious pores but small ball-like grains closely contacting with each other are observed in the compact surface morphology of the coating. Additionally, the columnar structure is unclear in the cross-section image of this coating. Thus, the $Al_xCr_{1-x}N$ coatings turn more compact with the decrease of $R\,(N_2)$, which is most likely due to an increase of Al content.

3.1.3. Hardness test

The hardness of the $Al_xCr_{1-x}N$ coatings increases with decreasing $R\,(N_2)$ from 20 to 6%, as presented in Fig. 7. This trend is related to the variation of lattice parameter, microstructure and grain size of $Al_xCr_{1-x}N$ coatings, and all of these correlate with different N_2 flow rates. Firstly, an increased Al content in the $Al_xCr_{1-x}N$ coatings with decreasing $R\,(N_2)$ can induce the lattice parameter of $Al_xCr_{1-x}N$ decreasing, which has been presented in Figs. 4 and 5, respectively. The decrease of lattice parameter with the addition of Al will increase the covalent energy in the coatings, which can result in an improved hardness of $Al_xCr_{1-x}N$ coatings [17,18]. Secondly, the $Al_xCr_{1-x}N$ coatings become more porous with increasing $R\,(N_2)$ (see Fig. 6), which can also induce a decrease of the hardness. Thirdly, the hardness of $Al_xCr_{1-x}N$ coatings increases with the decrease of $R\,(N_2)$, while the grain size of coatings decreases. Therefore, this variation trend is approximately consistent with the Hall–Petch relationship in which the decrease of grain size will result in hardness increasing [19].

Table 1
Atomic concentration of the $Al_xCr_{1-x}N$ coatings deposited at different $R\,(N_2)$.

Sample	$R\,(N_2)$ (%)	Content (at.%)			Al/(Al + Cr) (%)	Al/Cr
		Al	Cr	N		
1	20%	19.7	16.2	64.1	54.9	1.2
2	17%	21.2	15.9	62.9	57.1	1.3
3	13%	22.2	16.6	61.2	57.2	1.3
4	11%	24.8	15.2	60.0	62.0	1.6
5	8%	26.3	16.3	57.4	61.7	1.6
6	6%	31.9	16.5	51.6	65.4	1.9

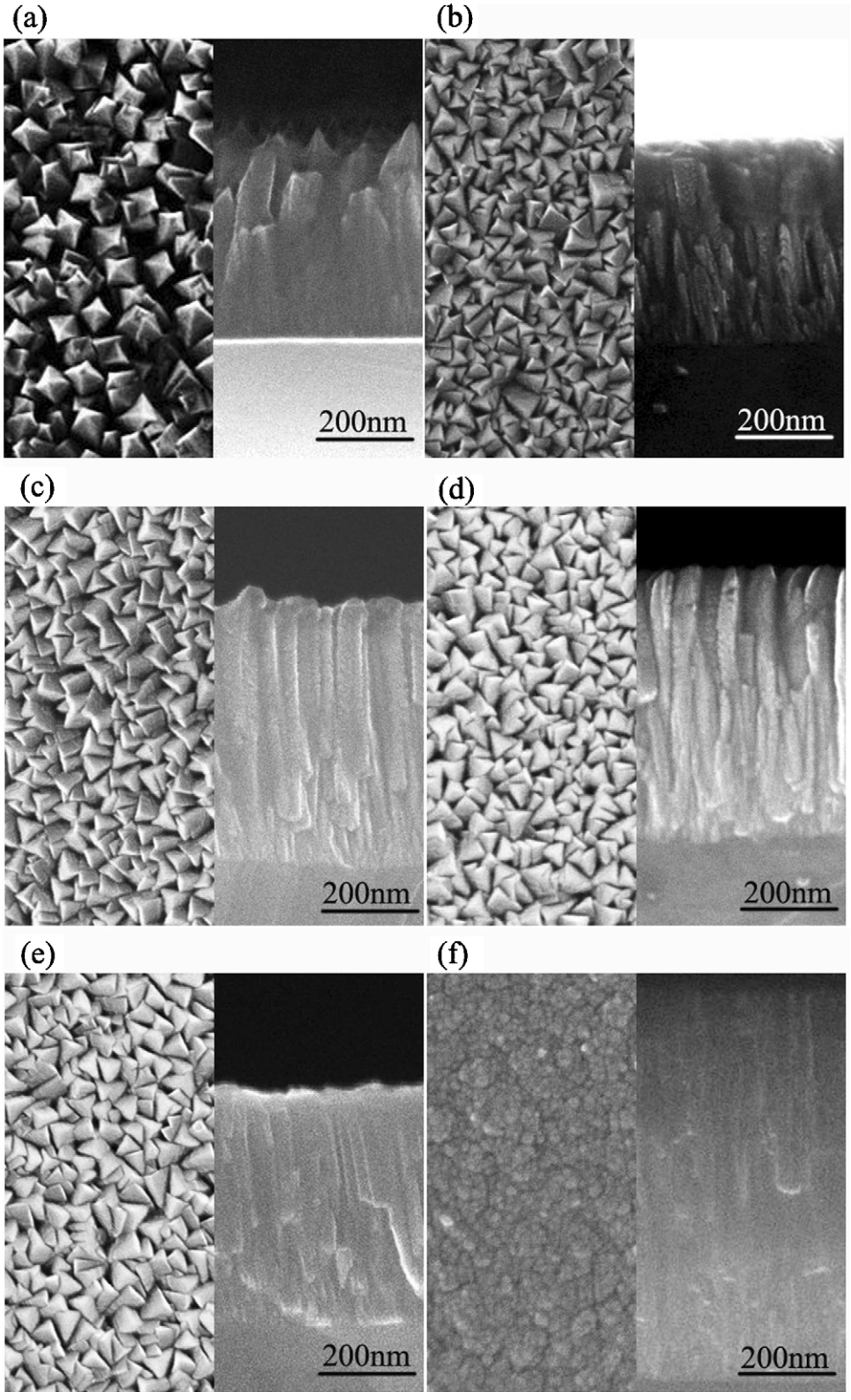

Fig. 6. SEM images of $Al_xCr_{1-x}N$ coatings prepared at $R(N_2)$ = (a) 20%, (b) 17%, (c) 13%, (d) 11%, (e) 8%, and (f) 6%. The right section of each figure shows the cross-section of each sample.

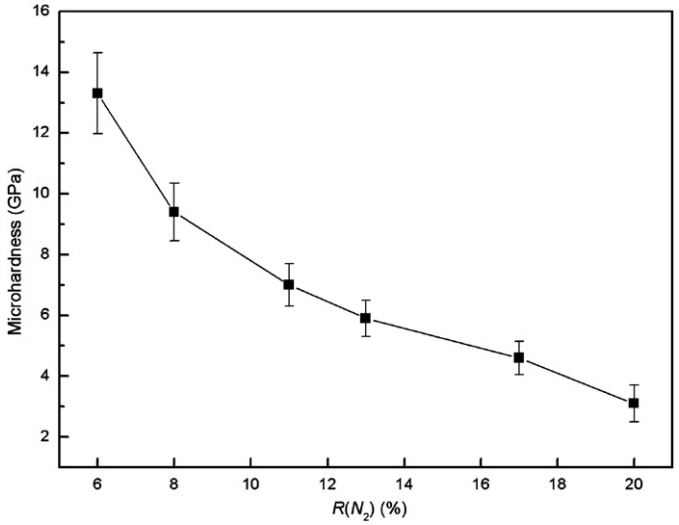

Fig. 7. Microhardness of $Al_xCr_{1-x}N$ coatings prepared at different $R(N_2)$.

3.2. Effect of working pressure on $Al_xCr_{1-x}N$ coatings

In order to study the effect of working pressure on $Al_xCr_{1-x}N$ coatings, the comparable experiments were carried out at an Ar flow rate of 40 sccm, and $R(N_2) = 11\%$. The working pressure changes from 0.4 to 2.0 Pa.

3.2.1. XRD and chemical composition analyses

The XRD patterns (Fig. 8) show that, the $Al_xCr_{1-x}N$ coatings exhibit mixed phases with a B1-NaCl cubic crystal structure and a B4-w-ZnS hexagonal crystal structure when P_w is less than 0.8 Pa, and then turn to a single phase with B1-NaCl cubic crystal structure when P_w exceeds 0.8 Pa.

The Al content and thickness of the $Al_xCr_{1-x}N$ coatings deposited at different P_w are shown in Fig. 9. The Al content of coatings decreases from 73.7 to 63.0 at.% with increasing P_w from 0.4 to 2.0 Pa. This result indicates that P_w can seriously affect the sputtering yield of Al target. At low P_w, the Al content of $Al_xCr_{1-x}N$ coatings is higher because of the larger sputtering yield of Al target, which would lead to the formation of mixed phases (cubic + hexagonal)

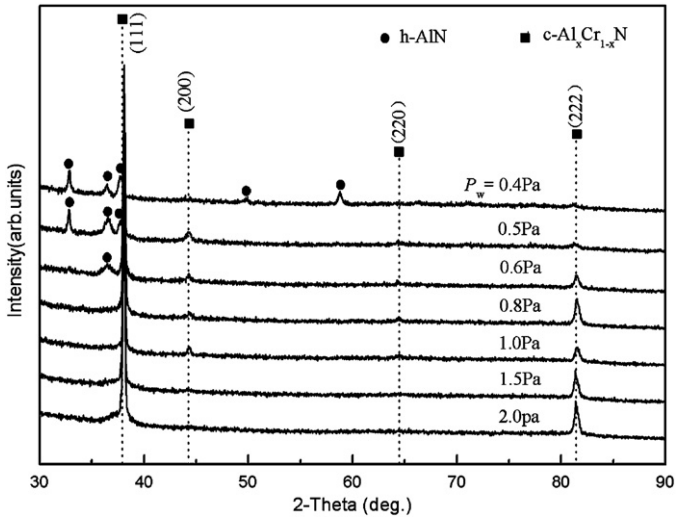

Fig. 8. XRD patterns of $Al_xCr_{1-x}N$ coatings prepared at different P_w.

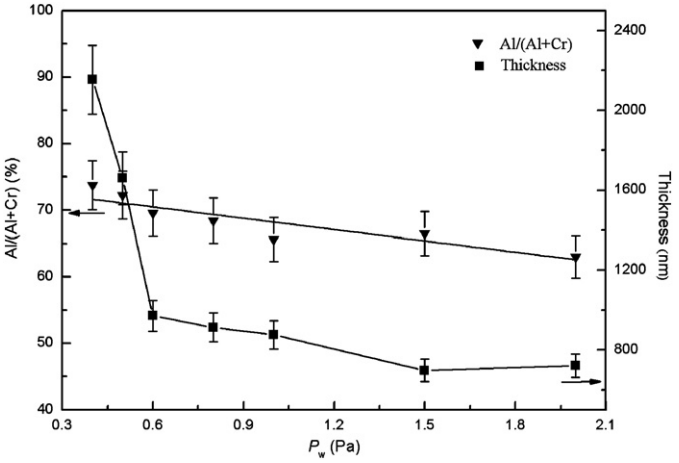

Fig. 9. Al content and thickness of $Al_xCr_{1-x}N$ coatings prepared at P_w.

in the coatings [17]. At $P_w = 0.8$ Pa, the Al content of the $Al_xCr_{1-x}N$ coating with a single phase (cubic) is 68.4 at.%. This value is very close to the maximum solubility of Al in $Al_xCr_{1-x}N$, approximately 71 at.% [5,20]. Since the formation of the metastable phase usually depends on the structural defects and orientation of films, the maximum solubility of Al in $Al_xCr_{1-x}N$ is different from the value of 77.2 at.% calculated by Sugishima et al. [21]. Accordingly, the thickness also reduces with the increase of P_w (in Fig. 9). In particular, there is a pronounced drop in thickness when increasing P_w from 0.4 to 0.8 Pa. This is mainly attributed to a reduced fraction of hexagonal phase which has higher specific volume than its cubic counterpart [14]. Moreover, the collision events of the sputtered species on their way to the substrate increase with increasing P_w, thus, the thickness of coatings decreases as less species will reach the substrate. When further increasing P_w from 0.8 to 2.0 Pa, the thickness of the coatings with single phase (cubic) continues to decrease, which is mainly induced by the increasing collision events of the sputtered species at higher P_w.

3.2.2. Microstructural morphology

Fig. 10 shows the SEM images of the $Al_xCr_{1-x}N$ coatings prepared at different P_w. When P_w is 0.4 Pa, grains on the surface of coating show rice-granule morphology and arrange compactly, though the size of grains is inhomogeneous. Improving P_w to 0.5 Pa makes the grains grow up to a stone-like morphology, contacting with each other closely. It can be clearly seen that the bulky ones are made up of some small grains. When P_w exceeds 0.6 Pa, all the acquired coatings exhibit sharp pyramid grains, and have more bulky grains and pores till $P_w = 2.0$ Pa. It can be seen from Fig. 10(c–d) that the $Al_xCr_{1-x}N$ coatings become relative porous with increasing P_w.

3.2.3. Hardness test

Fig. 11 shows the influence of working pressure on the hardness of $Al_xCr_{1-x}N$ coatings. The hardness increases with increasing P_w from 0.4 to 0.8 Pa, and reaches the maximum value at 0.8 Pa. Then, a further increase of P_w results in the decrease of hardness. This trend is related with Al content and phase composition of the $Al_xCr_{1-x}N$ coatings. At lower P_w (<0.8 Pa), Al content of coatings is higher than 70 at.% (Fig. 9), and a hexagonal phase is formed in $Al_xCr_{1-x}N$ coatings (Fig. 8). It has been reported that the hardness of $Al_xCr_{1-x}N$ coatings will decrease due to the formation of the hexagonal phase [17]. Therefore, the increase of hardness with increasing P_w (P_w <0.8 Pa) is attributed to a reduced fraction of hexagonal phase resulted form the decreased Al content. At $P_w = 0.8$ Pa, the

$Al_xCr_{1-x}N$ coating exhibits the highest hardness and a single cubic phase (Fig. 8), and its Al content (68.4 at.%) is very close to the maximum solubility of Al in $Al_xCr_{1-x}N$. With the further increase of P_w, all the $Al_xCr_{1-x}N$ coatings show a single cubic phase (Fig. 8), and the Al content of the coatings continues to decrease (Fig. 9). Thus, as discussed in Section 3.1.3, a decreased Al content will result in a decrease of hardness of $Al_xCr_{1-x}N$ coatings. Furthermore, the fact that the $Al_xCr_{1-x}N$ coatings become relatively porous and have more bulky grains (Fig. 10) will also induce a decrease of hardness when increasing P_w.

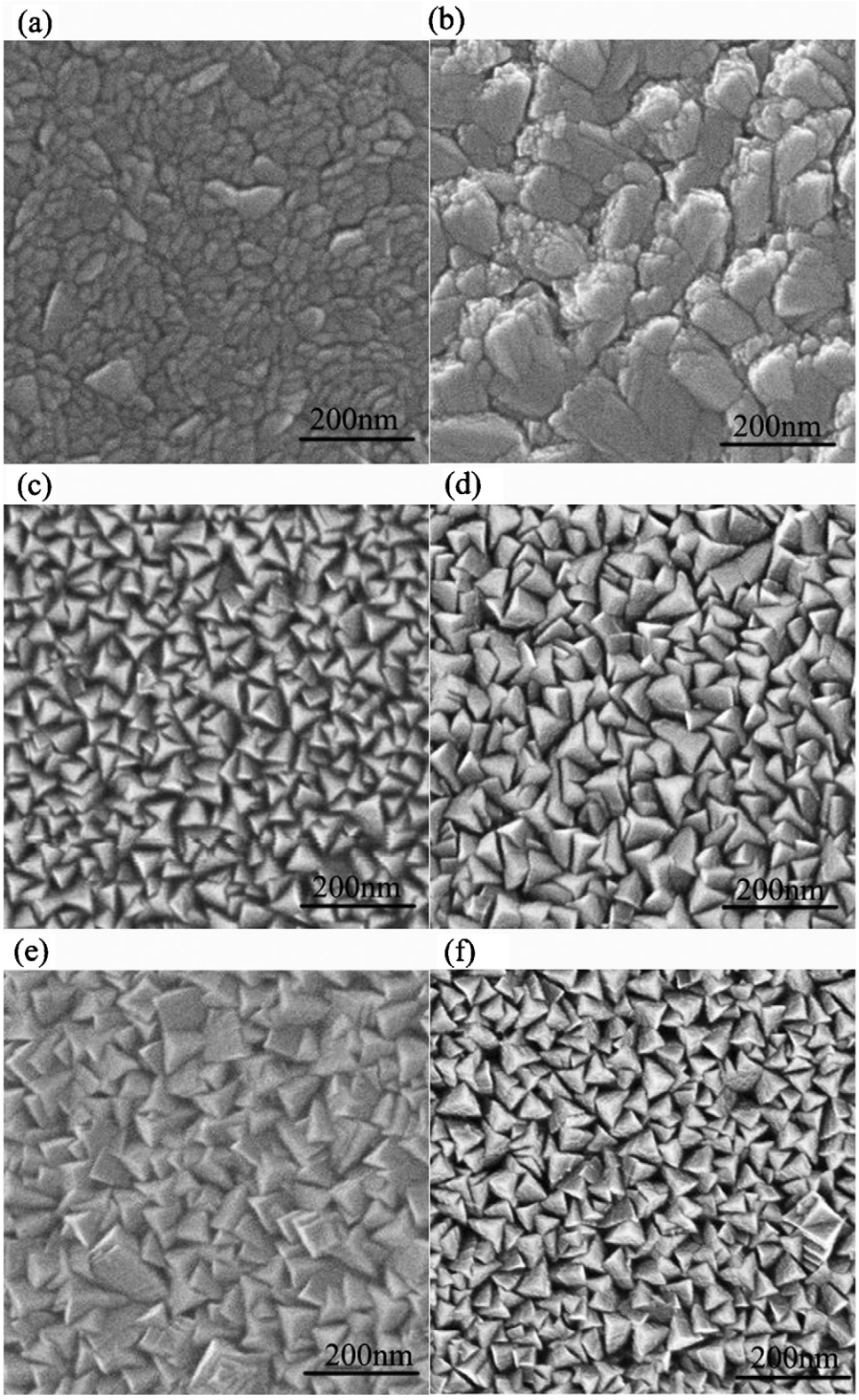

Fig. 10. SEM images of $Al_xCr_{1-x}N$ coatings prepared at different working pressure. (a) 0.4 Pa, (b) 0.5 Pa, (c) 0.6 Pa, (d) 1.0 Pa, (e) 1.5 Pa, and (f) 2.0 Pa.

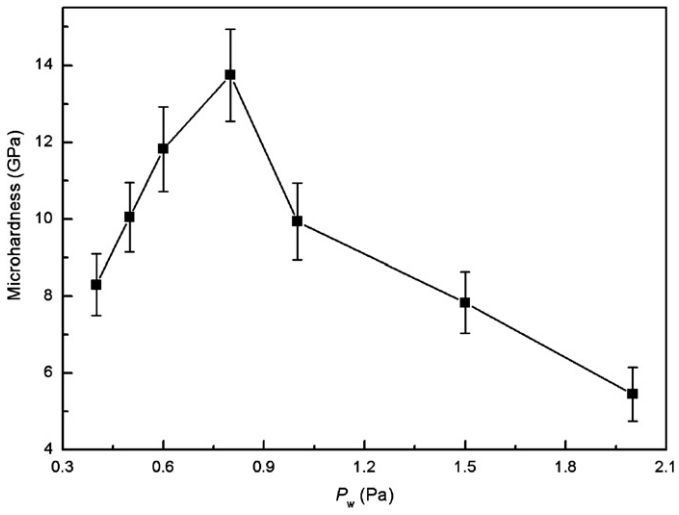

Fig. 11. Microhardness of $Al_xCr_{1-x}N$ coatings prepared at different P_w.

4. Conclusions

The $Al_xCr_{1-x}N$ coatings were deposited by a reactive magnetron co-sputtering system using DC power to Al target at different N_2 flow rates and working pressures. The influence of N_2 flow rate and working pressure on the structure and properties of the $Al_xCr_{1-x}N$ coatings has been analyzed and discussed. The results show that N_2 flow rate and working pressure can significantly affect the chemical and phase composition, grain size and microstructure of $Al_xCr_{1-x}N$ coatings. The columnar structure of the $Al_xCr_{1-x}N$ coatings gradually disappears with R (N_2) decreasing from 20 to 6%, and the coatings appear more compact at a low R (N_2). The $Al_xCr_{1-x}N$ coatings exhibit the highest hardness at R (N_2) = 6% and P_w = 0.8 Pa, respectively. Moreover, the obtained results obviously show that the $Al_xCr_{1-x}N$ coatings have the highest hardness values only when the prepared $Al_xCr_{1-x}N$ coatings exhibit a single cubic phase and the Al content is mostly closed to the maximum solubility of Al in $Al_xCr_{1-x}N$. Further work is underway to improve the properties of the present $Al_xCr_{1-x}N$ coatings.

Acknowledgements

The authors should thank Prof. Zhimei Sun and Dr. Yan Yu for English revision. This work was partially supported by the National Key Technology R&D Program of China (2007BAE05B04), and by the National Natural Science Foundation of China (No. 50825101 and No. 50971108).

References

[1] G.S. Kim, S.Y. Lee, J.H. Hahn, B.Y. Lee, J.G. Han, J.H. Lee, S.Y. Lee, Surf. Coat. Technol. 171 (2002) 83–90.
[2] C.S. Sandu, R. Sanjinés, M. Benkahoul, F. Medjani, F. Lévy, Surf. Coat. Technol. 201 (2006) 4083–4089.
[3] S. Veprek, M.J.G. Veprek-Heijman, Surf. Coat. Technol. 202 (2008) 5063–5073.
[4] H.C. Barshilia, N. Selvakumar, B. Deepthi, K.S. Rajam, Surf. Coat. Technol. 201 (2006) 2193–2201.
[5] P.H. Mayrhofer, H. Willmann, A.E. Reiter, Surf. Coat. Technol. 202 (2008) 4935–4938.
[6] H. Willmann, P.H. Mayrhofer, P.O.Å. Persson, A.E. Reiter, L. Hultman, C. Mitterer, Scripta Mater. 54 (2006) 1847–1865.
[7] J.L. Endrino, S. Palacín, M.H. Aguirre, A. Gutiérrez, F. Schäfers, Acta Mater. 55 (2007) 2129–2135.
[8] M. Holzherr, M. Falz, T. Schmidt, Surf. Coat. Technol. 203 (2008) 505–509.
[9] G.S. Kim, S.Y. Lee, Surf. Coat. Technol. 201 (2006) 4361–4366.
[10] T.P. Li, Y.C. Zhou, M.S. Li, Z.P. Li, Surf. Coat. Technol. 202 (2008) 1985–1993.
[11] M. Dopita, D. Rafaja, Ch. Wüstefeld, M. Růžička, V. Klemm, D. Heger, G. Schreiber, M. Šíma, Surf. Coat. Technol. 202 (2008) 3199–3207.
[12] L. Chen, M. Moser, Y. Du, P.H. Mayrhofer, Thin Solid Films 517 (2009) 6635–6641.
[13] D. Gall, S. Kodambaka, M.A. Wall, I. Petrov, J.E. Greene, J. Appl. Phys. 93 (2003) 9086–9094.
[14] D. Holec, F. Rovere, P.H. Mayrhofer, P.B. Barna, Scripta Mater. 62 (2010) 349–352.
[15] R.F. Zhang, S. Veprek, Mater. Sci. Eng. A 448 (1–2) (2007) 111–119.
[16] R.F. Zhang, S. Veprek, Acta Mater. 55 (2007) 4615–4624.
[17] J. Lin, B. Mishra, J.J. Moore, W.D. Sproul, Surf. Coat. Technol. 201 (2006) 44329–44334.
[18] M. Zhou, Y. Makino, M. Nose, K. Nogi, Thin Solid Films 339 (1999) 203–208.
[19] M. Hakamada, Y. Nakamota, H. Matsumoto, H. Iwasaki, Y. Chen, H. Kusuda, Mater. Sci. Eng. A 457 (2007) 120–126.
[20] A. Reiter, V. Derflinger, B. Hanselmann, T. Bachmann, B. Sartory, Surf. Coat. Technol. 200 (2005) 2114–2122.
[21] A. Sugishima, H. Kajioka, Y. Makino, Surf. Coat. Technol. 97 (1997) 590–594.